



FOREVER22: the first bright galaxies with Population III stars at redshifts $z \simeq 10$ – 20 and comparisons with *JWST* data

Hidenobu Yajima ¹, ¹★ Makito Abe,¹ Hajime Fukushima ¹, Yoshiaki Ono,² Yuichi Harikane,² Masami Ouchi,^{2,3,4} Takuya Hashimoto ⁵ and Sadegh Khochfar⁶

¹Center for Computational Sciences, University of Tsukuba, 1-1-1 Tennodai, Tsukuba, Ibaraki 305-8577, Japan

²Institute for Cosmic Ray Research, The University of Tokyo, 5-1-5 Kashiwanoha, Kashiwa, Chiba 277-8582, Japan

³Kavli IPMU (WPI), The University of Tokyo, 5-1-5 Kashiwanoha, Kashiwa, Chiba 277-8583, Japan

⁴National Astronomical Observatory of Japan, 2-21-1 Osawa, Mitaka, Tokyo 181-8588, Japan

⁵Tomonaga Center for the History of the Universe (TCHoU), Faculty of Pure and Applied Sciences, University of Tsukuba, Tsukuba, Ibaraki 305-8571, Japan

⁶Institute for Astronomy, University of Edinburgh, Royal Observatory, Edinburgh EH9 3HJ, UK

Accepted 2023 August 10. Received 2023 August 10; in original form 2022 November 22

ABSTRACT

We study the formation of the first galaxies in overdense regions modelled by the FORMation and EVolution of galaxies in Extremely overdense Regions motivated by SSA22 (FOREVER22) simulation project. Our simulations successfully reproduce the star formation rates and the M_{UV} – M_{star} relations of candidate galaxies at $z \sim 10$ – 14 observed by the *JWST*. We suggest that the observed galaxies are hosted by dark matter haloes with $M_h \gtrsim 10^{10} M_\odot$ and are in short-period starburst phases. On the other hand, even simulated massive galaxies in overdense regions cannot reproduce the intense star formation rates and the large stellar masses of observed candidates at $z \sim 16$. Also, we show that the contribution of Population III stars to the ultraviolet (UV) flux decreases as the stellar mass increases and it is a few per cent for galaxies with $M_{\text{star}} \sim 10^7 M_\odot$. Therefore, a part of the observed flux by *JWST* could be the light from Population III stars. Our simulations suggest that the UV flux can be dominated by Population III stars and the UV slope shows $\beta \lesssim -3$ if future observations would reach galaxies with $M_{\text{stars}} \sim 10^5 M_\odot$ at $z \sim 20$ of which the mass fraction of Population III stars can be greater than 10 per cent.

Key words: stars: Population III – galaxies: evolution – galaxies: formation – galaxies: high-redshift.

1 INTRODUCTION

Understanding galaxy formation is one of the central issues in current astrophysics. In particular, the first galaxies at redshifts beyond $z = 10$ are the most likely drivers of cosmic reionization (Yajima et al. 2009, 2014; Yajima, Choi & Nagamine 2011; Paardekooper, Khochfar & Dalla Vecchia 2013, 2015; Wise et al. 2014; Arata et al. 2019; Ma et al. 2020; Rosdahl et al. 2022) and hosts of the first massive black holes (Regan & Haehnelt 2009; Agarwal et al. 2014; Yajima & Khochfar 2016; Wise et al. 2019; Latif et al. 2022a). Thus, revealing the formation of the first galaxies is of great importance. Using Lyman α lines, a lot of galaxies at $z \lesssim 9$ have been identified (e.g. Ono et al. 2012; Shibuya et al. 2012; Finkelstein et al. 2013; Song et al. 2016; Ouchi et al. 2018). However, the transmission of the Lyman α line is reduced significantly as the neutral degree of the intergalactic medium increases, resulting in the difficulty of galaxy observation beyond $z \sim 10$ (Yajima, Sugimura & Hasegawa 2018). Recent submillimetre observations have successfully detected high-redshift galaxies at $z \lesssim 9$ via the detections of [C II] 158 μm and [O III] 88 μm lines (e.g. Capak et al. 2015; Inoue et al. 2016; Hashimoto et al. 2018; Tamura et al. 2019). The metal-line observation is expected to be difficult if target galaxies exceed $z \sim 10$ because of insufficient

metal enrichment (e.g. Baxx et al. 2023; Popping 2023; Yoon et al. 2023). Therefore, galaxies at $z \gtrsim 10$ have been investigated with Lyman-break technique (e.g. Oesch et al. 2013, 2016; Bouwens et al. 2019). However, the number of samples has been limited and the spectroscopic confirmations have been difficult for the sensitivities of the telescopes with a reasonable integration time.

These situations are drastically changing with observations by *JWST*. Using the data of the first cycle observation by *JWST*, high-redshift galaxies have been identified. Donnan et al. (2023) found 44 new candidate galaxies and estimated the ultraviolet (UV) luminosity functions at the redshifts $z = 8$ – 15 . Harikane et al. (2023) found candidate galaxies at $z \sim 16$ with large stellar masses and star formation rates (SFRs; see also Naidu et al. 2022). Furtak et al. (2023) indicated that the candidate galaxies at $z \sim 9$ – 16 had properties of young galaxies with ages ~ 10 – 100 Myr and very blue UV slope down to $\beta \sim -3$ (see also Topping et al. 2022; Cullen et al. 2023).

The properties of high-redshift galaxies at $z > 6$ have been investigated in various simulation projects as CODA (Ocvirk et al. 2016), FLARES (Lovell et al. 2021), THESAN (Kannan et al. 2022), MILLENIUMTNG (Pakmor et al. 2023), UNIVERSEMA-CHINE (Behroozi et al. 2019), and Santa Cruz model (Gabrielpillai et al. 2022). These simulations successfully reproduced statistical properties like luminosity functions of observed galaxies at $z \lesssim 8$. Also, some previous works provided theoretical predictions of galaxy properties at $z \gtrsim 10$ from the simulation results (e.g. Behroozi et al.

* E-mail: yajima@ccs.tsukuba.ac.jp

2020; Kannan et al. 2023). While these simulations allow us to study the statistical natures of high-redshift galaxies with large cosmic volumes, it is still difficult to study evolution from minihaloes hosting the Population III (Pop III) stars to massive galaxies due to the limited resolution.

In previous theoretical studies, galaxy formation at $z \gtrsim 10$ proceeds with the formation of Pop III stars, the radiative feedback, and the metal enrichment via the first supernovae (SNe; e.g. Maio et al. 2011; Wise et al. 2012; Johnson, Dalla & Khochfar 2013; Smith et al. 2015; Xu et al. 2016; Chiaki & Wise 2019). Because of the metal enrichment from Pop III stars, formation sites of new Pop III stars move from higher to lower density regions in large-scale structure (e.g. Tornatore, Ferrara & Schneider 2007; Pallottini et al. 2014; Xu et al. 2016; Liu & Bromm 2020). Such numerical simulations bridging from Pop III stars in minihaloes to first galaxies are still challenging. Jeon & Bromm (2019) investigated the formation of first galaxies with the halo mass of $M_h \sim 10^9 M_\odot$ at $z = 9$ and showed their observational properties. Abe et al. (2021) studied the impact of the initial mass function of Pop III stars on the physical properties of first galaxies with $M_h \sim 10^{8-9} M_\odot$. They showed that inducing frequent pair-instability SNe suppresses the gas mass fraction and the SFRs of the first galaxies significantly for the top-heavy initial mass function. The simulated halo masses in previous works have been limited to $\sim 10^9 M_\odot$. Therefore, the emergent UV fluxes were too faint for the sensitivities of current telescopes.

Considering the brightness of observed candidates at $z \gtrsim 10$, they can be hosted in massive haloes that likely form in overdense regions. In this work, we investigate galaxy formation in overdense regions in which the halo mass exceeds $10^{11} M_\odot$ at $z \sim 10$. To study the transition from Pop III to Population II (Pop II) stars, our simulations resolve minihaloes and follow their growth up to the massive haloes.

Our paper is organized as follows. Section 2 shows our methodology and the information about the simulation set-up. In Section 3, we show the star formation histories and compare them with the observational data by *JWST*. Also, we study the mass fraction of Pop III stars with regard to the total stellar mass. Finally, we summarize our results and discuss the limitations of our study in Section 4.

2 METHODOLOGY

We use the results of our simulation project FOREVER22 (Yajima et al. 2022) that focuses on protocluster regions in the cosmic volume of $(714 \text{ cMpc})^3$. In this project, we use the GADGET-3 code (Springel 2005) with subgrid models developed in the OWLS project (Schaye et al. 2010) and the FiBY project (Johnson et al. 2013). Besides, we newly updated the code by adding the photoionization feedback, the radiation pressure on dust, dust growth/destruction, black hole growth, and its feedback (see more in Yajima et al. 2022). The project consists of zoom-in simulations with three different levels of the mass resolution and the size of zoom-in regions: protocluster region [PCR; $V = (28.6 \text{ cMpc})^3$, smoothed particle hydrodynamics (SPH) particle mass, $m_{\text{SPH}} = 4.1 \times 10^6 M_\odot$, and final redshift, $z_{\text{end}} = 2.0$]; brightest protocluster galaxy [BCG; $V \sim (10 \text{ cMpc})^3$, $m_{\text{SPH}} = 5.0 \times 10^5 M_\odot$, and $z_{\text{end}} = 4.0$]; and First run [$V \sim (3 \text{ cMpc})^3$, $m_{\text{SPH}} = 7.9 \times 10^3 M_\odot$, and $z_{\text{end}} = 9.5$]. The PCR runs reproduce the observed SFR densities of protoclusters at $z \sim 2-6$. Also, we confirmed that the mean density fields reproduced the observed stellar mass functions, main sequences of star formation, gas fractions, and metallicities of galaxies as a function of stellar mass well (Yajima et al. 2022). In this work, we use First runs (First0 and First1 runs) in which the most massive halo reaches $M_h = 4.8 \times 10^{11} M_\odot$ at $z = 9.5$. The cosmological parameters are still under debate (Komatsu et al.

2011; Planck Collaboration VI 2020; Freedman 2021). Considering the changing history of the parameter and Hubble parameter tension (Freedman 2021), we adopt the cosmological parameters as $\Omega_M = 0.3$, $\Omega_b = 0.045$, $\Omega_\Lambda = 0.7$, $\sigma_8 = 0.82$, and $h = 0.7$.

In this work, we consider both Pop II and Pop III stars. If the metallicity is lower than a critical value, the initial mass function (IMF) is likely to be a top-heavy (e.g. Chon, Omukai & Schneider 2021). Besides, the effective temperature of Pop III stars is high $T \sim 10^5 \text{ K}$ (Schaerer 2002). Therefore, Pop III stars can be strong sources of radiative and SN feedback. We set the critical gas metallicity $Z = 1.5 \times 10^{-4} Z_\odot$ below which Pop III stars form (Omukai et al. 2005; Frebel, Johnson & Bromm 2007; Chon et al. 2021). Although the critical metallicity is still under debate, Abe et al. (2021) suggested that the physical properties of the first galaxies did not depend on it sensitively (see also Maio et al. 2010). We assume that the IMF of Pop III stars is $dn \propto M^{-2.35} dM$ with the mass range $21-500 M_\odot$, while that of Pop II is Chabrier IMF with the range $0.1-100 M_\odot$. Because of the expensive calculation costs for the first star formation with radiative and magnetic feedback, the IMF of Pop III stars is still under debate (Stacy & Bromm 2014; Susa, Hasegawa & Tominaga 2014; Hirano et al. 2015; Sugimura et al. 2020; Wollenberg et al. 2020; Latif, Whalen & Khochfar 2022b). Therefore, we adopt a simple power-law function for the IMF of Pop III stars.

In evaluating the SFR, we consider the star formation model based on the observed Kennicutt–Schmidt law that was developed in Schaye & Dalla Vecchia (2008). The local SFR is measured as $\dot{m}_{\text{star}} \propto m_{\text{gas}} A (1 M_\odot \text{ pc}^{-2})^{-n} (\frac{\gamma}{f_g} f_g P)^{(n-1)/2}$, where m_{gas} is the mass of a gas particle, $\gamma = 5/3$ is the ratio of specific heats, f_g is the gas mass fraction in the galactic disc, and P is the total interstellar medium (ISM) pressure. Here, we set $A = 1.5 \times 10^{-4} M_\odot \text{ yr}^{-1} \text{ kpc}^{-2}$ and $\gamma = 1.4$ for $n_H < 10^3 \text{ cm}^{-3}$ and $\gamma = 2.0$ for $n_H \geq 10^3 \text{ cm}^{-3}$. The star formation model is the same as in EAGLE simulation project (Schaye et al. 2015). Star formation occurs if local gas density exceeds $n_H = n_0 \text{ cm}^{-3} (\frac{Z}{0.002})^{-0.64}$, where we set $n_0 = 10.0$ for First runs. In the estimation of the net cooling rate, we follow the non-equilibrium chemistry of primordial gas and the equilibrium state of metals from pre-calculated tables with CLOUDY v07.02 code (Ferland 2000).

Once massive stars form, they give UV radiation feedback to surrounding gas within their lifetime $\sim 10^7 \text{ yr}$. We take into account the photoionization process of hydrogen and the dissociation of hydrogen molecules. We estimate the volume of the ionized region by taking the balance between the photon production rate and the total recombination rate as (see the detail in Abe et al. 2021; Yajima et al. 2022)

$$\dot{N}_{\text{ion}} = \sum_{i=1}^n \alpha_B n_{\text{H II}}^i n_e^i \frac{m_{\text{gas}}^i}{\rho_{\text{gas}}^i}, \quad (1)$$

where \dot{N}_{ion} is the photon production rate of a stellar particle, α_B is the case-B recombination coefficient, $n_{\text{H II}}^i$ and n_e^i are the ionized hydrogen and electron number densities of i th SPH particle. In the ionized regions, the gas temperature is heated up to $3 \times 10^4 \text{ K}$, and star formation is prohibited. The dissociation rate of hydrogen molecules is evaluated based on the contributions of stars in the calculation box. First, we measure UV fluxes from stars with distances to a target gas particle as

$$J_{\text{LW},21} = \sum_{i=1}^n f_{\text{LW}} \left(\frac{r_i}{1 \text{ kpc}} \right)^{-2} \left(\frac{m_{*,i}}{10^3 M_\odot} \right), \quad (2)$$

where $J_{\text{LW},21}$ is described in unit of $10^{-21} \text{ erg s}^{-1} \text{ cm}^{-2} \text{ Hz}^{-1} \text{ sr}^{-1}$, r_i is the distance from i th stellar particle to a target gas particle and

$m_{*,i}$ is the mass of i th stellar particle. Then, we take into account the self-shielding effect with the local H_2 density and Jeans length (Johnson et al. 2013):

$$N_{\text{H}_2} = 2 \times 10^{15} \text{ cm}^{-2} \left(\frac{f_{\text{H}_2}}{10^{-6}} \right) \left(\frac{n_{\text{H}}}{10 \text{ cm}^{-3}} \right)^{1/2} \left(\frac{T}{10^3 \text{ K}} \right)^{1/2}, \quad (3)$$

where f_{H_2} is the fraction of H_2 and n_{H} is the hydrogen number density. We consider the shielding factor derived in Wolcott-Green, Haiman & Bryan (2011) as

$$f_{\text{shield}}(N_{\text{H}_2}, T) = \frac{0.965}{(1+x/b_5)^{1.1}} + \frac{0.035}{(1+x)^{0.5}} \times \exp[-8.5 \times 10^{-4}(1+x)^{0.5}], \quad (4)$$

where $x \equiv N_{\text{H}_2}/5 \times 10^{14} \text{ cm}^{-2}$ and $b_5 \equiv b/10^5 \text{ cm s}^{-1}$. Here b is the Doppler broadening parameter, $b \equiv (k_{\text{B}}T/m_{\text{H}})^{1/2}$. Thus, we estimate the H_2 dissociation rate (κ_{diss}) by combining $J_{\text{LW},21}$ and f_{shield} as $\kappa_{\text{diss}} \propto f_{\text{shield}} J_{\text{LW},21}$. In addition, we consider the photodetachment process of H^- (Shang, Bryan & Haiman 2010). With the dissociation and formation rates, we evaluate H_2 abundance and its radiative cooling rate that is a main factor in controlling the formation of Pop III stars in minihaloes.

When the age of a stellar particle reaches 10^7 yr , SN feedback turns on. Following the SN feedback model in Dalla Vecchia & Schaye (2012), we stochastically select a neighbouring gas particle and heat the temperature up to $10^{7.5} \text{ K}$. This hot bubble rapidly expands and induces galactic wind, resulting in the suppression of star formation.

3 RESULTS

Fig. 1 shows the column density maps of gas and stars. Stellar distributions are smoothed with a point spread function of *JWST*. The gas widely distributes within virial radii, while stellar distributions are compact and concentrated at the galactic centres. The gas accretes onto galaxies along the filamentary structures and the stellar feedback disturbs the gas structure. Stellar distributions and sizes change with time. At $z = 12$, stellar clumps distribute at $0.5 R_{\text{vir}}$, which reflects the minor merger phase. As the galaxy grows via baryon accretion, the size of the stellar components increases, but becomes small rapidly when major mergers happen (see also Ono et al. 2023). Note that the size shrinkage after the merger process sensitively depends on the gas fraction and the structure of progenitor galaxies (e.g. Dekel & Cox 2006).

Fig. 2 presents the redshift evolution of halo, stellar masses, and SFR. The halo masses of the main progenitors are $\sim 10^9 M_{\odot}$ at $z \sim 20$ and evolve to $\sim 10^{11.5} M_{\odot}$ at $z \sim 10$. The fluctuations are due to mergers and the ability of the friends-of-friends (FoF) group finder to identify all member particles. The rarity of the halo with $10^{11.5} M_{\odot}$ at $z = 10$ is $dN/d \ln M_{\text{h}} \sim 2 \times 10^{-7} \text{ cMpc}^{-3}$. The cosmic volume to host such a massive halo in our simulations is $\sim 500 \text{ cMpc}^3$ that is similar to the volumes of photometric galaxy surveys with *JWST* (e.g. Finkelstein et al. 2023). Therefore, it can be reasonable to directly compare our simulations with *JWST* data. Note that the rarity changes with time even for the most massive progenitors in the same region because of the variety of the halo merger history.

As the halo grows, the stellar mass increases. The stellar masses of the main progenitors exceed $10^8 M_{\odot}$ at $z \sim 13(14)$ and finally reach $4.3(6.8) \times 10^9 M_{\odot}$ in First0 (First1) run. The stellar masses are similar to observed galaxies at $z \lesssim 12$. On the other hand, it is much lower than the observed ones at $z \sim 16$. Suppose the estimated stellar masses of observed candidates are accurate and the

redshifts are actually ~ 16 . In that case, most gas is very efficiently converted into stars even in the early Universe (Harikane et al. 2023). Inayoshi et al. (2022) suggested that 0.1–0.3 of the gas should be converted into stars by using the abundance-matching technique with the observed UV luminosity functions. In our simulations, the SN feedback efficiently works in the suppression of star formation. As a result, the gas is gradually converted into stars, and the star formation efficiency ($M_{\text{star}}/M_{\text{gas}}$) of main progenitors in First0 run is 1.1×10^{-1} , 2.0×10^{-2} , and 2.5×10^{-2} at $z = 10, 14$, and 17 . Note that the redshifts and the physical properties of the candidate galaxies at $z > 14$ were estimated with the photometric data. It is difficult to evaluate the impacts of emission lines only from the photometric data (e.g. Schaerer & de Barros 2009). Therefore, their properties can be changed with follow-up spectroscopy (e.g. Arrabal Haro et al. 2023).

The SFR also increases with the growth of halo mass. Because of the cycle of suppression of star formation and the short recovery time-scale of gas, the SFR fluctuates significantly with time (Yajima et al. 2017). Main progenitor galaxies can have $\gtrsim 10 M_{\odot} \text{ yr}^{-1}$ at $z \lesssim 14$ and show starbursts with $\text{SFR} = 50.4 (133.5) M_{\odot} \text{ yr}^{-1}$ at $z = 9.5$ in First0 (First1) run. If we consider the SFR as $\text{SFR} = \epsilon \frac{M_{\text{gas}}}{\tau_{\text{dyn}}}$, where ϵ is an efficiency parameter and τ_{dyn} is the dynamical time, the starbursts at $z \sim 9.5$ correspond to $\epsilon \sim 0.08\text{--}0.25$. This value is much larger than typical star-forming galaxies in the local Universe. In the last period of 0.1 Gyr ($z = 9.5\text{--}11.5$), the halo mass of the main progenitors in First0 run increases from $1.2 \times 10^{11} M_{\odot}$ to $4.8 \times 10^{11} M_{\odot}$. The rapid mass growth with major mergers can induce the starburst. The SFRs at $z \lesssim 14$ nicely match with the observed ones by *JWST* (Naidu et al. 2022; Donnan et al. 2023; Harikane et al. 2023) and GN-z11 at $z = 10.957$ (Jiang et al. 2021). Also, the modelled galaxies reproduce the observed M_{UV} at those redshifts. As suggested in Yajima et al. (2017), once the halo mass exceeds $10^{11} M_{\odot}$, most gas can be trapped in the deep gravitational potential against SN feedback. This can induce the starburst with $\text{SFR} \gtrsim 10 M_{\odot} \text{ yr}^{-1}$ and make galaxies observable. In the redshift range, black holes are still in the state of being initial seeds with $\sim 10^5 M_{\odot}$ and the accretion rates are mostly much lower than the Eddington limit. Therefore, active galactic nucleus (AGN) feedback is negligible.

Fig. 3 presents SFRs as a function of stellar mass. The SFR increases with the stellar mass. At $M_{\text{star}} \lesssim 10^8 M_{\odot}$, the suppression of SFR due to the feedback makes the large dispersion. On the other hand, massive galaxies keep the star formation continuous. We confirm that our results match the observed galaxies. The stellar mass monotonically increases with the halo mass, although there is a large dispersion. The ratios of stellar to halo mass are $\sim 10^{-3}$ and $\sim 10^{-2}$ for $M_{\text{h}} = 10^{10}$ and $10^{11} M_{\odot}$ at $z = 10$. These values are similar to the empirical models in UNIVERSEMACHINE project (Behroozi et al. 2020), while it is somewhat higher than MILLENIUMTNG (Kannan et al. 2023). The conversion efficiency sensitively depends on the resolution, the star formation, and the feedback models. In particular, our simulations can resolve minihaloes and dwarf galaxies, and their star formation. At high redshifts, stars formed in dwarf galaxies can contribute to the stellar mass in more massive galaxies via frequent merger processes.

We present the relationships between the UV flux M_{UV} and the halo and the stellar mass in Fig. 4. We estimate M_{UV} by measuring the mean UV flux densities at $\lambda = 1500\text{--}2000 \text{ \AA}$ in modelled spectral energy distributions (SEDs) that will be shown in Fig. 6. M_{UV} is tightly related to the SFR, although it somewhat changes depending on the star formation history. As the halo mass increases, the SFR becomes higher, resulting in the formation of bright galaxies. We find that the brightness can exceed the observable level $M_{\text{UV}} \lesssim -18 \text{ mag}$,

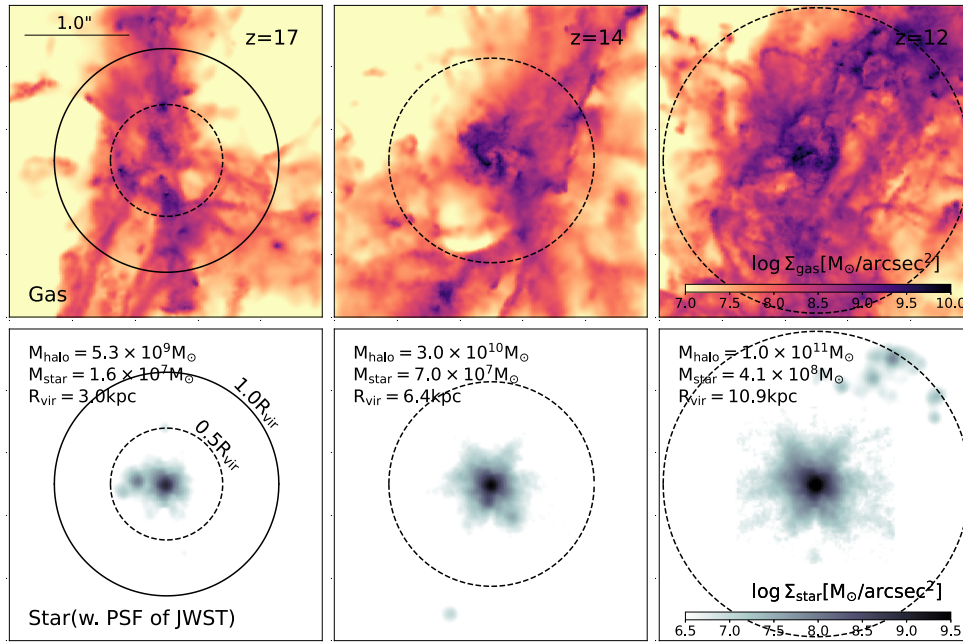


Figure 1. Column density maps of gas and stars in the most massive progenitors at $z = 12, 14,$ and 17 . The stellar distributions are smoothed with the point spread function of *JWST*. Halo (stellar) masses are 5.3×10^9 (1.6×10^7) M_\odot at $z = 17$, 3.0×10^{10} (7.0×10^7) M_\odot at $z = 14$, and 1.0×10^{11} (4.1×10^8) M_\odot at $z = 12$. Solid and dashed circles represent virial radii and half-virial radii, respectively. The size of the boxes is 3 arcsec, corresponding to $L = 11.0, 9.8,$ and 8.4 physical kpc at $z = 12, 14,$ and 17 .

if the halo mass is larger than $\sim 10^{10} M_\odot$. In low-mass haloes, galaxies at higher redshifts form stars more efficiently because they are compact and have higher gas density typically. Also, there is a large dispersion. This can be due to the SN feedback that induces the intermittent star formation history via the cycle of gas inflow and outflow (Yajima et al. 2017). On the other hand, the UV brightness is more tightly correlated with the stellar mass. Our simulations reproduce the observed UV brightnesses nicely. Galaxies with $M_{\text{star}} \gtrsim 10^8 M_\odot$ are likely to have observable UV brightness $M_{\text{UV}} \lesssim -18$ mag. As shown in Fig. 2, the SFR rapidly increases as the halo mass increases. Therefore, the stellar masses in the massive haloes can be contributed mainly by the current starburst episode, resulting in the tight relation in the massive systems. Note that some observed galaxies with $M_{\text{star}} \sim 10^{6-7} M_\odot$ are brighter than our modelled galaxies, although they are within the error bars. As one possibility, hidden faint AGNs might contribute to observe UV fluxes (e.g. Bunker et al. 2023). Future deep spectroscopic studies will allow us to investigate AGN activities.

The upper panel of Fig. 5 shows the mass fraction of young Pop III stars to the total stellar mass. As the star formation proceeds, the interstellar gas is metal enriched via Type II SNe. Therefore, the fraction steeply decreases as the stellar mass increases. Also, some fractions of galaxies have no young Pop III stars. This indicates Pop III stars form only when primordial gas clouds accrete on a galaxy. Once the stellar mass exceeds $\sim 10^7 M_\odot$, the fraction becomes $\lesssim 0.01$. Considering the sensitivities of current telescopes, only massive galaxies with $M_{\text{star}} \gtrsim 10^7 M_\odot$ have been observed. Therefore, Pop II stars mainly form in the observed candidate galaxies at $z \gtrsim 10$. We find that the mass fraction is insensitive to the redshift in the range of $z = 10-20$. Given that the metal production source is only Type II SNe, the total metal mass released is simply proportional to the stellar mass. Thus, the insensitive redshift dependence indicates similar metal mixing with the interstellar gas in the redshift range.

Our simulations suggest that low-mass galaxies with $M_{\text{star}} \lesssim 10^5 M_\odot$ host Pop III stars with non-negligible fraction $\gtrsim 0.1$. Recently, Riaz, Hartwig & Latif (2022) showed the mass fraction of Pop III stars to the total stellar masses based on their seminumerical models (Hartwig et al. 2022). The mass fraction of low-mass galaxies with $M_{\text{star}} \sim 10^{4-5} M_\odot$ is similar to their results. On the other hand, our results for massive galaxies are much higher. Our cosmological simulations indicate that the gas in minihaloes can survive as the primordial state and contribute to the Pop III star formation in massive galaxies.

The lower panel of Fig. 5 represents the contribution of Pop III stars to the UV flux at $\lambda = 1500 \text{ \AA}$ in a rest frame. The contribution fraction also decreases with the mass of Pop III stars. However, since the mass-to-light ratio of Pop III stars is large and their effective temperature is high $T \sim 10^5 \text{ K}$ (Schaerer 2002), the contribution is moderately large even if the mass fraction of Pop III stars is low. In the cases of $M_{\text{star}} \sim 10^7 M_\odot$, it can be a few per cent. Therefore, a part of the observed fluxes by *JWST* could be contributed by Pop III stars. The UV flux can be dominated by Pop III stars if the stellar mass is lower than $\sim 10^5 M_\odot$. However, the low-mass systems are likely to be too faint for the sensitivities of current telescopes. Therefore, next-generation telescopes or gravitationally lensed galaxies by foreground sources might be required for direct observations of Pop III star clusters. Very recently, Vanzella et al. (2023) indicated a candidate of a Pop III star cluster with the mass of $\lesssim 10^4 M_\odot$ with the gravitational lens effect. The total metallicity even for low-mass galaxies with $M_{\text{star}} \lesssim 10^5 M_\odot$ exceeds $\sim 10^{-3} Z/Z_\odot$. Therefore, the formation of Pop III stars indicates inhomogeneous metal enrichment in a galaxy. The formation sites of Pop III stars are somewhat far from the high-density regions of Pop II stars where the metal enrichment proceeds earlier. Also, we find that the number fraction of galaxies hosting young Pop III stars increases from ~ 0.3 for $M_{\text{star}} = 10^5 M_\odot$ to ~ 0.7 for $M_{\text{star}} = 10^8 M_\odot$. The low-

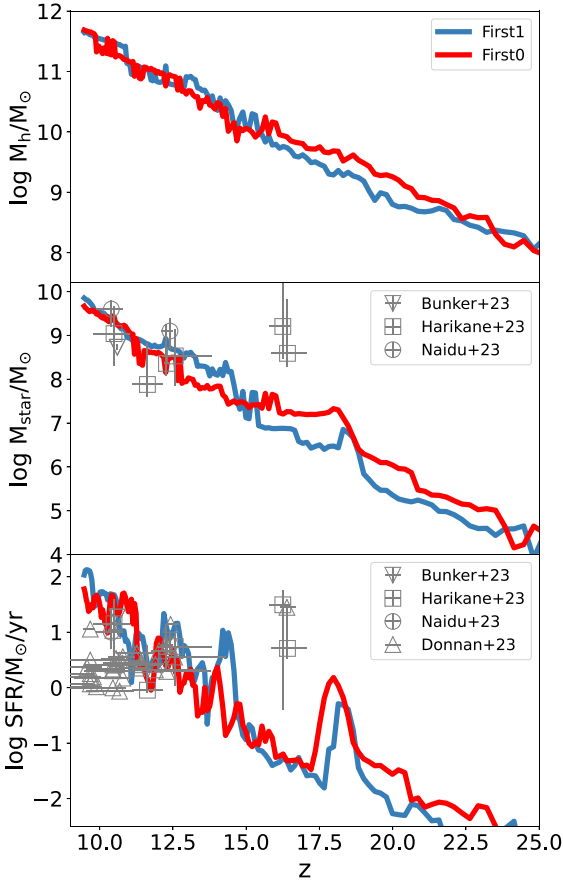


Figure 2. Redshift evolution of the halo, stellar mass, and SFR. The red and blue lines represent the properties of the most massive progenitors in First0 and First1 runs, respectively. Open symbols show the observations: inverted triangles (Bunker et al. 2023), squares (Harikane et al. 2023), circles (Naidu et al. 2022), and triangles (Donnan et al. 2023).

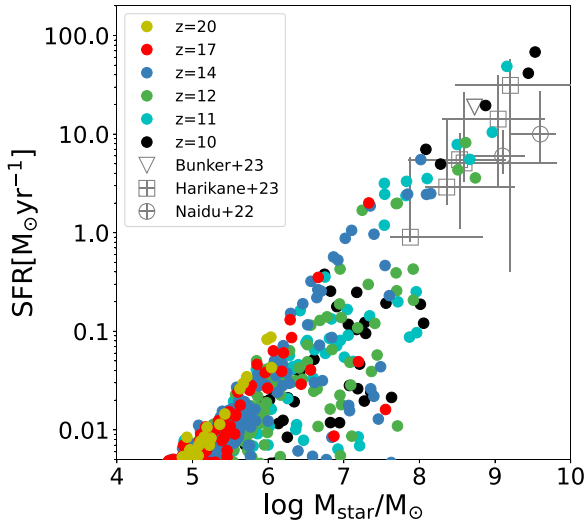


Figure 3. SFRs as a function of stellar mass. Filled circles are our simulation results. Different colours represent the different redshifts. Open symbols show the observational data: squares (Harikane et al. 2023), circles (Naidu et al. 2022), and inverted triangles (Bunker et al. 2023).

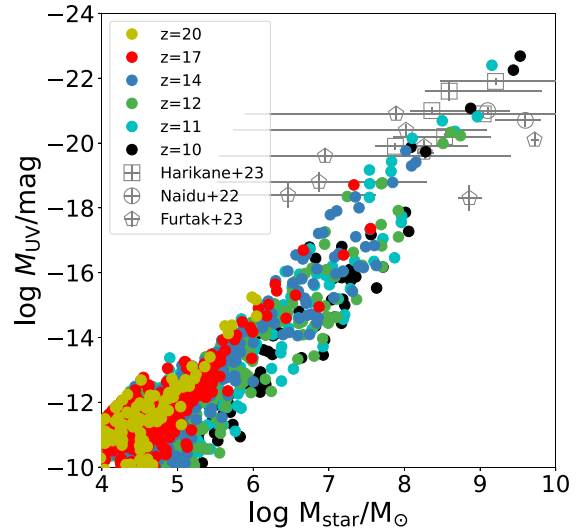
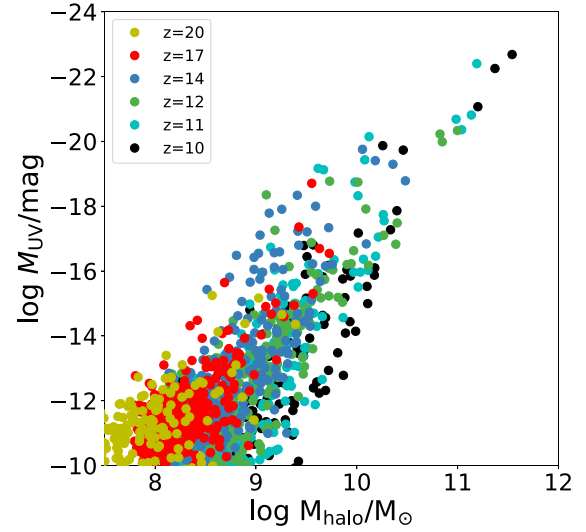


Figure 4. UV fluxes as a function of halo and stellar masses. Filled circles are our simulation results. Different colours represent the different redshifts. Open symbols show the observational data: squares (Harikane et al. 2023), circles (Naidu et al. 2022), and pentagons (Furtak et al. 2023).

mass galaxies without young Pop III stars consist of two states: star forming only with Pop II stars and quenching of star formation due to the SN feedback. Massive haloes are likely to distribute near the centre of overdense regions and primordial gas hosted by minihaloes can accrete them frequently. Therefore, the massive haloes can host young Pop III stars although the mass fraction is low.

Note that even for the Pop III stars, we model the star formation by replacing a gas particle with a stellar particle with the uniform mass $\sim 8 \times 10^3 M_\odot$, which models a star cluster. Therefore, the stellar particles release the same SN energy and metal mass. However, if the total stellar mass is smaller than $\sim 10^3 M_\odot$ in low-mass haloes, the IMF may not be universal, resulting in unequal SN feedback and metal amount (Abe et al. 2021). This can enhance spatial fluctuation of metal distribution in the large cosmic volume. Therefore, the metal distributions in low-mass galaxies are likely to change with the resolution and the model of Pop III stars. We will

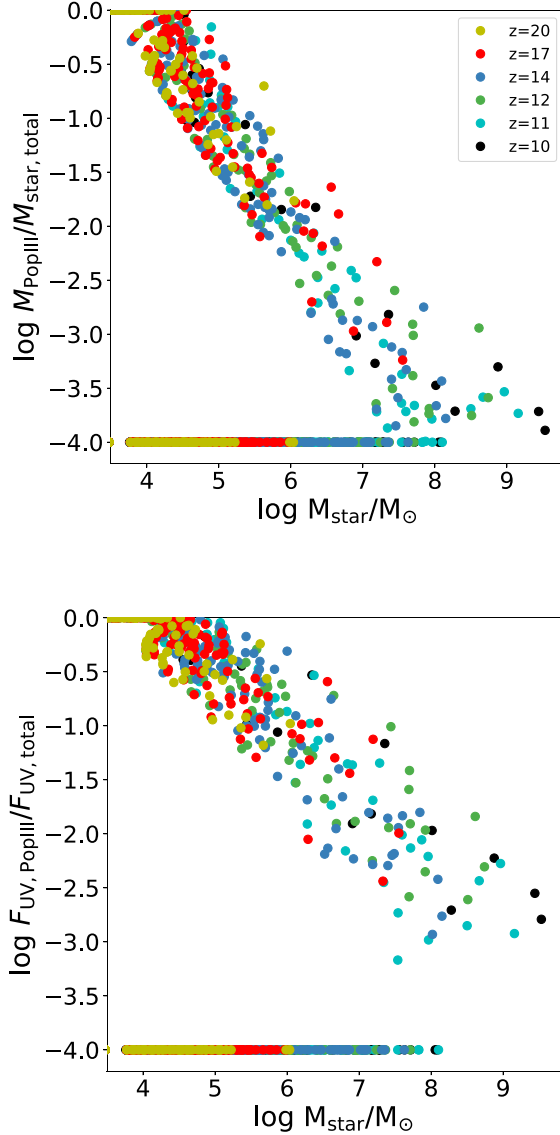


Figure 5. Mass fraction of young Pop III stars to the total stellar mass (upper panel) and their contribution fraction to UV flux at $\lambda = 1500 \text{ \AA}$ in the rest frame (lower panel). Different colours represent the different redshifts. The galaxies with mass fractions lower than 10^{-4} are plotted at -4.0 .

investigate these impacts on the fraction of Pop III stars in future work.

Here, we derive intrinsic SEDs of galaxies by using a stellar synthesis code STARBURST99 (Leitherer et al. 1999). Fig. 6 shows the SEDs of the most massive progenitors at $z = 12, 14, 17,$ and 20 . In this work, we estimate SEDs with the optically thin approximation, i.e. no dust attenuation, which can be reasonable for low-mass and low-metallicity galaxies (Yajima et al. 2012, 2014; Cullen et al. 2017). The observed blue UV slope ($\beta \lesssim -2$) supports the assumption (Naidu et al. 2022; Furtak et al. 2023). The contribution from Pop III stars is estimated with the assumption of the brightness temperature of 10^5 K and the mass-to-luminosity ratio for $120 M_{\odot}$ derived in Schaerer (2002). The mass fractions of Pop III stars of the galaxies are $1.1 \times 10^{-3}, 1.8 \times 10^{-3}, 4.7 \times 10^{-3},$ and 0.2 at $z = 12, 14, 17,$ and 20 , respectively. Their contributions to UV luminosity densities at $\lambda = 1500 \text{ \AA}$ are $1.4 \times 10^{-2}, 1.6 \times 10^{-2}, 7.5 \times 10^{-2},$ and 0.57 . We find that the contribution fraction can be

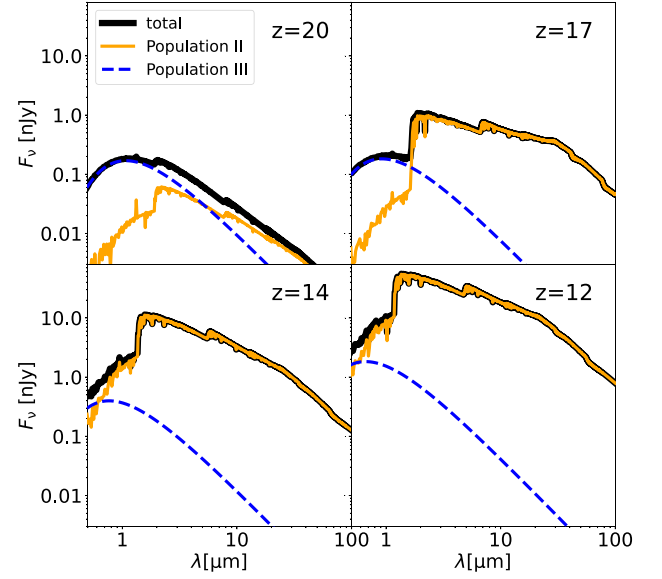


Figure 6. SEDs of the most massive progenitors at $z = 12, 14, 17,$ and 20 . Blue dashed and orange solid lines show the radiation only from Pop III and Pop II stars, respectively. Black solid lines are SEDs considering both stellar populations.

fit by $\log_{10} f_{\text{UV, Pop III}} = 0.66 \log_{10} \left(\frac{M_{\text{star, Pop III}}}{M_{\text{star}}} \right) + 0.20$. At $z = 20$, the light from Pop III stars dominates at UV wavelengths. At the lower redshifts, the UV-continuum fluxes are dominated by Pop II stars. We measure the UV slopes of the SEDs by using the flux densities at $\lambda = 1300, 2000,$ and 3000 \AA . It shows $\beta = -2.68, -2.76, -2.62,$ and -3.33 at $z = 12, 14, 17,$ and 20 , respectively. These naturally reproduce the very blue slopes of the observed galaxies (Atek et al. 2023; Furtak et al. 2023). Note that we do not consider the nebular emission in the above SEDs. If the nebular continuum at the UV wavelengths is added into the SEDs, the slopes are changed to $\beta = -2.55, -2.60, -2.57,$ and -2.98 at $z = 12, 14, 17,$ and 20 . Furthermore, dust extinction can make the SEDs redder at lower redshifts.

The galaxies at $z \leq 14$ have UV flux densities of $\gtrsim 10 \text{ nJy}$ that are observable by *JWST* with a reasonable integration time. We suggest that a part of the observed fluxes of candidate galaxies at $z \gtrsim 10$ could be contributed by Pop III stars. If the sensitivity of future observations at $3 \mu\text{m}$ will reach $\sim 0.1 \text{ nJy}$, the UV light dominated by Pop III stars can be observed directly. Also, note that Lyman-continuum (LyC) fluxes can be dominated by Pop III stars significantly even if the mass fraction of Pop III stars is low, $\lesssim 0.1$. For example, the contribution of Pop III stars to the LyC flux at 900 \AA for the galaxy at $z = 17$ is 0.7 . Thus, these galaxies consisting of both Pop II and Pop III stars can be strong ionizing sources. In addition, they may have unique properties in SEDs with high equivalent widths of doubly ionized oxygen, carbon, and helium (see also Nakajima & Maiolino 2022). In this work, we do not take into account the radiative transfer in the galaxies. However, since the galaxies are low-mass and low-metallicity systems, non-ionizing UV-continuum photons are expected to escape efficiently. Therefore, the estimated UV slopes are unlikely to change significantly. On the other hand, the escape fraction of LyC photons can change with time depending on the inhomogeneous gas structure due to the SN feedback (Yajima et al. 2014; Paardekooper, Khochfar & Dalla Vecchia 2015; Kimm et al. 2016; Trebitsch et al. 2017). In

the case of a high escape fraction, He II and other metal lines can be faint. As shown in Ono et al. (2023), the sizes of our modelled galaxies change with time significantly. In phases when dusty gas compactly distributes star-forming regions at the galactic centre, UV photons can be attenuated even at such high redshifts. In practice, the gas at the galactic centre reaches a metallicity with $Z \gtrsim 0.1 Z_{\odot}$ at $z \sim 10$ (see also Isoe et al. 2023). The escape fraction of photons sensitively depends on the covering fraction of dusty gas clouds from young stars. We will perform radiative transfer simulations in future work.

4 DISCUSSION AND SUMMARY

We have investigated the star formation and physical properties in the first galaxies formed in overdense regions modelled by the FOREVER22 simulation project. Our simulations followed the evolution from minihaloes hosting Pop III stars to massive galaxies with $M_h > 10^{11} M_{\odot}$. Our findings are summarized as follows.

(i) SFR increases with the halo mass and changes in the short-time period due to the SN feedback. Once the halo mass exceeds $\sim 10^{11} M_{\odot}$, galaxies continuously form stars with $\text{SFR} \gtrsim 10 M_{\odot} \text{ yr}^{-1}$ and induce starbursts with $\sim 100 M_{\odot} \text{ yr}^{-1}$. Even massive galaxies in overdense regions cannot reproduce the observed stellar masses and SFRs of candidate galaxies at $z \sim 16$ suggested by Donnan et al. (2023), Harikane et al. (2023), and Naidu et al. (2022).

(ii) Our simulations reproduce the relation between M_{UV} and M_{star} of the observed galaxies at $z \gtrsim 10$ nicely. The galaxies with $M_{\text{star}} \gtrsim 10^8 M_{\odot}$ show UV brightness of $\lesssim -18$ mag that is observable by *JWST*.

(iii) Even when the galaxy is metal enriched and forms Pop II stars, Pop III stars can form in zero-metallicity spots. The mass fraction of Pop III stars decreases as the stellar mass increases, and it is < 0.01 for galaxies with $M_{\text{star}} \sim 10^7 M_{\odot}$. Therefore, candidate galaxies at $z \gtrsim 10$ by *JWST* can be dominated by Pop II stars. We suggest that a part of galaxies with $M_{\text{star}} \lesssim 10^5 M_{\odot}$ can host Pop III stars with a non-negligible fraction $\gtrsim 0.1$.

(iv) We model SEDs of galaxies with Pop II and Pop III stars. The UV-continuum fluxes of massive galaxies at $z \leq 17$ are dominated by Pop II stars. However, a few per cent of UV fluxes can be from Pop III stars because of their large mass-to-luminosity ratio. The galaxies at $z \leq 14$ have the brightness of $\gtrsim 10$ nJy at $\lambda = 2 \mu\text{m}$ that can be observable by *JWST* with a reasonable integration time.

The estimated physical properties and redshifts of the observed galaxies at $z \gtrsim 10$ are not robust. Future spectroscopic observations would present more reliable data and constrain the physical properties of galaxies. On the other hand, the physical properties of first galaxies modelled by numerical simulations can depend on the resolution and the models of star formation and feedback (Abe et al. 2021). Also, the seeding of the first massive black holes is still under debate (Inayoshi, Visbal & Haiman 2020), and it may change the physical properties of galaxies and SEDs. The star formation efficiency of massive haloes with $M_h \gtrsim 10^{10} M_{\odot}$ at $z \sim 10$ is similar to the results in Behroozi et al. (2020) and somewhat higher than Kannan et al. (2023). In this paper, we newly provide insights about the relationship between Pop III stars and massive galaxies at $z \gtrsim 10$. The physical properties are likely to sensitively depend on the resolution, the star formation, and the feedback models. We will investigate the model and resolution dependencies on the first galaxy formation in future work.

ACKNOWLEDGEMENTS

The numerical simulations were performed on the computer cluster, XC50 in NAOJ, and Trinity at Center for Computational Sciences in University of Tsukuba. This work is supported in part by MEXT/JSPS KAKENHI Grant Numbers 17H04827, 20H04724, 21H04489 (HY), 20K22358, 22H01258 (TH), NAOJ ALMA Scientific Research Grant Number 2019–11A, JST FOREST Program, Grant Number JP-MJFR202Z, and Astro Biology Center Project research AB041008 (HY). For the purpose of open access, the author has applied a Creative Commons Attribution (CC BY) licence to any author accepted manuscript version arising from this submission.

DATA AVAILABILITY

The data underlying this paper will be shared on reasonable request to the corresponding author.

REFERENCES

- Abe M., Yajima H., Khochfar S., Dalla Vecchia C., Omukai K., 2021, *MNRAS*, 508, 3226
- Agarwal B., Dalla Vecchia C., Johnson J. L., Khochfar S., Paardekooper J.-P., 2014, *MNRAS*, 443, 648
- Arata S., Yajima H., Nagamine K., Li Y., Khochfar S., 2019, *MNRAS*, 488, 2629
- Arrabal Haro P. et al., 2023, preprint (arXiv:2303.15431)
- Atek H. et al., 2023, *MNRAS*, 519, 1201
- Bakx T. J. L. C. et al., 2023, *MNRAS*, 519, 5076
- Behroozi P. et al., 2020, *MNRAS*, 499, 5702
- Behroozi P., Wechsler R. H., Hearin A. P., Conroy C., 2019, *MNRAS*, 488, 3143
- Bouwens R. J., Stefanon M., Oesch P. A., Illingworth G. D., Nanayakkara T., Roberts-Borsani G., Labbé I., Smit R., 2019, *ApJ*, 880, 25
- Bunker A. J. et al., 2023, preprint (arXiv:2302.07256)
- Capak P. L. et al., 2015, *Nature*, 522, 455
- Chiaki G., Wise J. H., 2019, *MNRAS*, 482, 3933
- Chon S., Omukai K., Schneider R., 2021, *MNRAS*, 508, 4175
- Cullen F. et al., 2023, *MNRAS*, 520, 14
- Cullen F., McLure R. J., Khochfar S., Dunlop J. S., Dalla Vecchia C., 2017, *MNRAS*, 470, 3006
- Dalla Vecchia C., Schaye J., 2012, *MNRAS*, 426, 140
- Dekel A., Cox T. J., 2006, *MNRAS*, 370, 1445
- Donnan C. T. et al., 2023, *MNRAS*, 518, 6011
- Ferland G. J., 2000, *Rev. Mex. Astron. Astrofis. Ser. Conf.*, 9, 153
- Finkelstein S. L. et al., 2013, *Nature*, 502, 524
- Finkelstein S. L. et al., 2023, *ApJ*, 946, L13
- Frebel A., Johnson J. L., Bromm V., 2007, *MNRAS*, 380, L40
- Freedman W. L., 2021, *ApJ*, 919, 16
- Furtak L. J., Shuntov M., Atek H., Zitrin A., Richard J., Lehnert M. D., Chevallard J., 2023, *MNRAS*, 519, 3064
- Gabrielpillai A., Somerville R. S., Genel S., Rodriguez-Gomez V., Pandya V., Yung L. Y. A., Hernquist L., 2022, *MNRAS*, 517, 6091
- Harikane Y. et al., 2023, *ApJS*, 265, 5
- Hartwig T. et al., 2022, *ApJ*, 936, 45
- Hashimoto T. et al., 2018, *Nature*, 557, 392
- Hirano S., Hosokawa T., Yoshida N., Omukai K., Yorke H. W., 2015, *MNRAS*, 448, 568
- Inayoshi K., Harikane Y., Inoue A. K., Li W., Ho L. C., 2022, *ApJ*, 938, L10
- Inayoshi K., Visbal E., Haiman Z., 2020, *ARA&A*, 58, 27
- Inoue A. K. et al., 2016, *Science*, 352, 1559
- Isoe Y. et al., 2023, preprint (arXiv:2307.00710)
- Jeon M., Bromm V., 2019, *MNRAS*, 485, 5939
- Jiang L. et al., 2021, *Nat. Astron.*, 5, 256
- Johnson J. L., Dalla V. C., Khochfar S., 2013, *MNRAS*, 428, 1857
- Kannan R. et al., 2023, *MNRAS*, 524, 2594

- Kannan R., Garaldi E., Smith A., Pakmor R., Springel V., Vogelsberger M., Hernquist L., 2022, *MNRAS*, 511, 4005
- Kimm T., Cen R., Rosdahl J., Yi S., 2016, *ApJ*, 823, 52
- Komatsu E. et al., 2011, *ApJS*, 192, 18
- Latif M. A., Whalen D. J., Khochfar S., Herrington N. P., Woods T. E., 2022a, *Nature*, 607, 48
- Latif M. A., Whalen D., Khochfar S., 2022b, *ApJ*, 925, 28
- Leitherer C. et al., 1999, *ApJS*, 123, 3
- Liu B., Bromm V., 2020, *MNRAS*, 497, 2839
- Lovell C. C., Vijayan A. P., Thomas P. A., Wilkins S. M., Barnes D. J., Irodoto D., Roper W., 2021, *MNRAS*, 500, 2127
- Ma X., Quataert E., Wetzel A., Hopkins P. F., Faucher-Giguère C.-A., Kereš D., 2020, *MNRAS*, 498, 2001
- Maio U., Ciardi B., Dolag K., Tornatore L., Khochfar S., 2010, *MNRAS*, 407, 1003
- Maio U., Khochfar S., Johnson J. L., Ciardi B., 2011, *MNRAS*, 414, 1145
- Naidu R. P. et al., 2022, *ApJ*, 940, L14
- Nakajima K., Maiolino R., 2022, *MNRAS*, 513, 5134
- Ocvirk P. et al., 2016, *MNRAS*, 463, 1462
- Oesch P. A. et al., 2013, *ApJ*, 773, 75
- Oesch P. A. et al., 2016, *ApJ*, 819, 129
- Omukai K., Tsuribe T., Schneider R., Ferrara A., 2005, *ApJ*, 626, 627
- Ono Y. et al., 2012, *ApJ*, 744, 83
- Ono Y. et al., 2023, *ApJ*, 951, 72
- Ouchi M. et al., 2018, *PASJ*, 70, S13
- Paardekooper J.-P., Khochfar S., Dalla Vecchia C., 2013, *MNRAS*, 429, L94
- Paardekooper J.-P., Khochfar S., Dalla Vecchia C., 2015, *MNRAS*, 451, 2544
- Pakmor R. et al., 2023, *MNRAS*, 524, 2539
- Pallottini A., Ferrara A., Gallerani S., Salvadori S., D’Odorico V., 2014, *MNRAS*, 440, 2498
- Planck Collaboration VI, 2020, *A&A*, 641, A6
- Popping G., 2023, *A&A*, 669, L8
- Regan J. A., Haehnelt M. G., 2009, *MNRAS*, 396, 343
- Riaz S., Hartwig T., Latif M. A., 2022, *ApJ*, 937, L6
- Rosdahl J. et al., 2022, *MNRAS*, 515, 2386
- Schaerer D., 2002, *A&A*, 382, 28
- Schaerer D., de Barros S., 2009, *A&A*, 502, 423
- Schaye J. et al., 2010, *MNRAS*, 402, 1536
- Schaye J. et al., 2015, *MNRAS*, 446, 521
- Schaye J., Dalla Vecchia C., 2008, *MNRAS*, 383, 1210
- Shang C., Bryan G. L., Haiman Z., 2010, *MNRAS*, 402, 1249
- Shibuya T., Kashikawa N., Ota K., Iye M., Ouchi M., Furusawa H., Shimasaku K., Hattori T., 2012, *ApJ*, 752, 114
- Smith B. D., Wise J. H., O’Shea B. W., Norman M. L., Khochfar S., 2015, *MNRAS*, 452, 2822
- Song M., Finkelstein S. L., Livermore R. C., Capak P. L., Dickinson M., Fontana A., 2016, *ApJ*, 826, 113
- Springel V., 2005, *MNRAS*, 364, 1105
- Stacy A., Bromm V., 2014, *ApJ*, 785, 73
- Sugimura K., Matsumoto T., Hosokawa T., Hirano S., Omukai K., 2020, *ApJ*, 892, L14
- Susa H., Hasegawa K., Tominaga N., 2014, *ApJ*, 792, 32
- Tamura Y. et al., 2019, *ApJ*, 874, 27
- Topping M. W., Stark D. P., Endsley R., Plat A., Whittle L., Chen Z., Charlton S., 2022, *ApJ*, 941, 153
- Tornatore L., Ferrara A., Schneider R., 2007, *MNRAS*, 382, 945
- Trebitsch M., Blaizot J., Rosdahl J., Devriendt J., Slyz A., 2017, *MNRAS*, 470, 224
- Vanzella E. et al., 2023, preprint (arXiv:2305.14413)
- Wise J. H., Demchenko V. G., Halicek M. T., Norman M. L., Turk M. J., Abel T., Smith B. D., 2014, *MNRAS*, 442, 2560
- Wise J. H., Regan J. A., O’Shea B. W., Norman M. L., Downes T. P., Xu H., 2019, *Nature*, 566, 85
- Wise J. H., Turk M. J., Norman M. L., Abel T., 2012, *ApJ*, 745, 50
- Wolcott-Green J., Haiman Z., Bryan G. L., 2011, *MNRAS*, 418, 838
- Wollenberg K. M. J., Glover S. C. O., Clark P. C., Klessen R. S., 2020, *MNRAS*, 494, 1871
- Xu H., Norman M. L., O’Shea B. W., Wise J. H., 2016, *ApJ*, 823, 140
- Yajima H. et al., 2022, *MNRAS*, 509, 4037
- Yajima H., Choi J.-H., Nagamine K., 2011, *MNRAS*, 412, 411
- Yajima H., Khochfar S., 2016, *MNRAS*, 457, 2423
- Yajima H., Li Y., Zhu Q., Abel T., 2012, *MNRAS*, 424, 884
- Yajima H., Li Y., Zhu Q., Abel T., Gronwall C., Ciardullo R., 2014, *MNRAS*, 440, 776
- Yajima H., Nagamine K., Zhu Q., Khochfar S., Dalla Vecchia C., 2017, *ApJ*, 846, 30
- Yajima H., Sugimura K., Hasegawa K., 2018, *MNRAS*, 477, 5406
- Yajima H., Umemura M., Mori M., Nakamoto T., 2009, *MNRAS*, 398, 715
- Yoon I. et al., 2023, *ApJ*, 950, 61

This paper has been typeset from a $\text{\TeX}/\text{\LaTeX}$ file prepared by the author.